Effect of margin curvature on plate deformation in a 3-D numerical model of subduction zones

M. A. Bonnardot, R. Hassani, E. Tric, E. Ruellan, M. Regnier

Geophys. J. Int. (2008) **173,** 1084–1094 doi: 10.1111/j.1365-246X.2008.03752.x

Effect of margin curvature on plate deformation in a 3-D numerical model of subduction zones

M.-A. Bonnardot,[1] R. Hassani,[2] E. Tric,[1] E. Ruellan[1] and M. Régnier[1]

[1] *Laboratoire Géosciences Azur, Université Nice-Sophia Antipolis, Centre National de la Recherche Scientifique (C.N.R.S.), Observatoire Côte d'Azur, Institut de Recherche pour le Développement (I.R.D.),* 250 *av. Albert Einstein,* 06560 *Valbonne, France. E-mail: bonnardot@geoazur.unice.fr*

[2] *Laboratoire de Géophysique Interne et de Tectonophysique, CNRS, Université de Savoie, Campus Scientifique, Bâtiment "Le Chablais",* 73376 *Le Bourget du Lac Cédex, France*

Accepted 2007 February 5. Received 2007 February 5; in original form 2007 September 13

SUMMARY

The large amount of data acquired along most subduction zones underlines the importance of three dimensions in the subduction mechanism. In this work we use a fully 3-D mechanical numerical model to analyse the impact of the plate boundary geometry on the deformation of the upper plate. The model consists of two initially horizontal independent plates overlying an inviscid fluid and continuously pushed towards each other. The initial geometry of the contact zone between the two plates controls the stress regime and the strain pattern in the upper plate. The case with a linear plate boundary and orthogonal convergence is first considered and used as a reference model. With this simple model, the effects of some important parameters (i.e. the interplate friction and the lithosphere–asthenosphere density contrast) are investigated. Finally, cases with curved plate boundaries are considered, and the results are used to shed light on the importance of the dip direction of the interplate plane for the upper plate strain pattern. Unnecessary oceanward convexity causes an accumulation of the subducted material beneath the upper plate and induces an important uplift of the convex area. On the contrary, the material escapes from an oceanward concavity and provokes subsidence in the forearc zone. Such a behaviour induces preferential zones of weakeness in the overriding plate and may allow for explaining some local stress regime variations along convergent margins.

Key words: Numerical approximation and analysis; Subduction zone processes; Back-arc basin processes; Dynamics of lithosphere and mantle.

1 INTRODUCTION

Oceanic subduction is a complex geodynamic process responsible for most of the large lithospheric deformation observed at the surface of the Earth. These deformations result from various interactions between the two involved lithospheric plates and between the subducting plate and the asthenospheric mantle flow. The similarities observed in different subduction zones led Uyeda & Kanamori (1979) to propose two major types of subduction, the Marianas- and the Chile-types. These types are respectively defined by an extensional and a compressive tectonic regime within the overriding plate. A larger amount of surveyed data allowed Jarrard (1986) and more recently Heuret & Lallemand (2005), Lallemand *et al.* (2005) and Sdrolias & Muller (2006) to refine this classification and to statistically identify the main parameters controlling the tectonic regime within the overriding plate.

In addition to the field data, the understanding of the subduction process greatly evolved through the laboratory and numerical modelling. Various rheological laws based on a fluid dynamics or solid mechanics approach are currently used with success to better resolved the complex interactions between the asthenospheric mantle and the slab behaviour (i.e. Van Hunen *et al.* 2000; Billen *et al.* 2003; Funiciello *et al.* 2003; Arcay *et al.* 2005; Schellart 2005; Piromallo *et al.* 2006; Morra & Regenauer-Lieb 2006; Stegman *et al.* 2006) and/or the overriding plate deformations (i.e. Shemenda 1993, 1994; Hassani *et al.* 1997; Buiter 2000; Gardi *et al.* 2003; Govers & Wortel 2005; Sobolev & Babeyko 2005). Although some parameters, such as the plates velocity, the plate nature/density, the plates coupling or the subducting plate density show a particular relationship with the slab dip and tectonic regime (Scholz & Campos 1995; Hassani *et al.* 1997; Conrad *et al.* 2004; Lallemand *et al.* 2005; De Franco *et al.* 2006; Sdrolias & Muller 2006; Faccenna *et al.* 2007; Manea & Gurnis 2007), several segments of subduction zones remain out of the adopted classification. Examples include the anomalously high Altiplano in the Bolivian Orocline (Schellart *et al.* 2007), the along-strike variations of the dip angle of the Pacific subducting plate and some local variations of the tectonic regime observed in most of the upper plates.

Difficulties associated with classifying segments may come from the fact that most subduction models were established in 2-D and therefore neglected the lateral variations of the system. Recent simulation techniques now include the third dimension and can be used

to re-assess some of the unresolved geodynamic questions, which appear to be key issues in the global understanding of the subduction process.

Up to now, the studies considering a 3-D geometry were mainly devoted to the feedbacks between the mantle flow and the slab in order to better understand slab dip variations, trench retreat and the resulting dynamic topography (Funiciello *et al.* 2003; Husson 2006; Morra & Regenauer-Lieb 2006; Morra *et al.* 2006; Piromallo *et al.* 2006; Royden & Husson 2006; Stegman *et al.* 2006). However, they used either a viscous fluid approach or they neglected the overriding plate. Thus, the brittle behaviour of the overriding lithosphere and the mechanical coupling between both of the lithospheric plates involved in the surface deformation processes are not consider in their approach.

A 3-D solid mechanical approach including some interactions between the both lithospheric plates was proposed by Govers & Wortel (2005) to study the propagation of the lithosphere tearing. However, their method can only provide an instantaneous response of the system to the body forces and boundary conditions.

In this contribution, we study the upper plate deformation related to lithosphere–lithosphere coupling, by focusing more precisely on the effects of the margin curvature. We did not attempt to explain the origin of the arc curvature that may results from various phenomena and was already discussed by many authors (Frank 1968; Vogt 1973; Vogt *et al.* 1976; Hager & O'Connell 1978; Tovish & Schubert 1978; Hager & O'Connell 1979; Yamaoka *et al.* 1986; Mantovani *et al.* 2001; Schellart & Lister 2004; Morra *et al.* 2006; Schellart *et al.* 2007), but instead we aim at resolving the effects of some along-strike variations of the margin geometry on the upper plate tectonic. To carry out this investigation we used a modified version of the ADELI 2-D numerical code (Hassani *et al.* 1997) that was expanded in 3-D.

2 MECHANICAL AND NUMERICAL MODELLING

The 3-D model consists of two lithospheric plates of density ρ_l separated by a predefined fault and overlying an asthenospheric mantle of density ρ_a. This modelling only focuses on the first stages of the subduction process (<7 Ma), from the beginning of the downgoing motion to the moment when the slab reaches the bottom of the upper mantle. At this time scale temperature the effect can be neglected and owing to the high viscosity contrast between lithosphere and asthenosphere, the plates behave like a solid medium while the upper mantle can be seen as a fluid material. Moreover, as in Shemenda (1993) or Hassani *et al.* (1997) we make the strong assumption that this fluid is inviscid. We use this simplification of the problem, since solid–fluid coupling problems are difficult to address and require special developments (see Morra & Regenauer-Lieb 2006; Bonnardot *et al.* submitted). However, the asthenosphere is characterized by a low value of viscosity below the oceans ($\sim 10^{19}$ Pa s) (Cadek & Fleitout 2003) and some recent simulations defining the slab behaviour with respect to the mantle viscosity (Bonnardot *et al.* submitted) have shown that for asthenosphere viscosity values $\leq 10^{19}$ Pa s, no significant variations of the slab dip and of the stresses transmitted to the upper plate were observed between an inviscid and a low viscous asthenosphere. We consider that these results may support our strong assumption. Consequently, the interaction of the asthenosphere on the lithosphere may be reduced to an hydrostatic pressure which acts on each part of the lithosphere boundary in contact with the fluid.

2.1 Governing equations

Because the inertial effects are negligible the time evolution of the model is governed by a quasi-static problem which consists finding the vector field $\boldsymbol{v} : \Omega_t \rightarrow \mathbb{R}^3$ and the symetric tensor field $\boldsymbol{\sigma} : \Omega_t \rightarrow \mathrm{S}^{3\times 3}$ satisfying

$$\begin{cases} \mathbf{div}\boldsymbol{\sigma} + \rho_l \boldsymbol{g} = \mathbf{0} & \text{in } \Omega \\ \frac{D\boldsymbol{\sigma}}{Dt} = \mathcal{M}(\boldsymbol{\sigma}, \boldsymbol{d}) & \text{in } \Omega, \end{cases} \tag{1}$$

where $\Omega \subset \mathbb{R}^3$ is the physical domain occupied by the plates, $\boldsymbol{\sigma}$ is the Cauchy stress tensor, $\boldsymbol{v}$ is the velocity vector, $\boldsymbol{g}$ is the acceleration vector due to gravity, ρ_l is the lithosphere density and $d = \frac{1}{2}(\nabla \boldsymbol{v} + \nabla \boldsymbol{v}^T)$ is the Eulerian strain rate tensor (Mandel 1966; Noll 1972; Marsden & Hughes 1983). $\frac{D}{Dt}$ is an objective time derivative introduced in the context of large strain and/or large displacement to ensure material invariance through rigid body motion. The functional $\mathcal{M}$ stands for a general constitutive law.

In addition, unilateral constraints must be taken into account on the contact area Γ (subduction plan) between the two plates. These constraints, given by the Signorini relation (no interpenetration condition) and the Coulomb friction law, read:

$$\begin{cases} \delta v_n \leq 0, \quad \sigma_n \leq 0, \quad \delta v_n \sigma_n = 0, \\ \| \boldsymbol{\sigma}_t \| \leq -\mu \sigma_n \quad \text{if } \delta \boldsymbol{v}_t = 0, \\ \boldsymbol{\sigma}_t = \mu \sigma_n \frac{\delta \boldsymbol{v}_t}{\| \delta \boldsymbol{v}_t \|} \quad \text{if } \delta \boldsymbol{v}_t \neq 0, \end{cases} \tag{2}$$

where δv_n and $\delta \boldsymbol{v}_t$ are, respectively, the normal and tangential components of the relative velocity between a point of one plate and its projection onto the other plate, μ is the effective Coulomb friction coefficient (assumed constant throughout the contact interface) and σ_n and σ_t are the normal and tangential stresses, respectively (Jean & Touzot 1988).

2.2 Geometry, boundary conditions and constitutive laws

The two plates are initially horizontal and are separated by a dipping fault plane, $\alpha = 30^\circ$ (Fig. 1). The horizontal dimensions of the whole mechanical model are 1000 km long and 500 km wide. The problem (1)–(2) is solved with the following boundary conditions (see also Fig. 1): (1) an hydrostatic pressure P_a is acting on each part of the lithosphere in contact with the asthenospheric fluid and (2) a zero normal velocity is applied on all vertical edges excepted on that of the downgoing plate where a normal velocity of 6 cm yr^{-1} is prescribed.

Because the plates are compressible, the density contrast $\rho_l - \rho_a$ between an element of the slab and an element of the incompressible surrounding mantle would increase in an unrealistic way as the element goes down. A compressibility modulus β is therefore introduced for the upper mantle and the state equations are integrated to give the density and the pressure distribution in the asthenosphere:

$$\begin{cases} \rho_a(z) = \rho_a^0 / \left(1 - \beta \rho_a^0 g z\right) \\ P_a(z) = -\dfrac{1}{\beta} \ln\left(1 - \beta \rho_a^0 g z\right), \end{cases} \tag{3}$$

where $g = \|\boldsymbol{g}\|$ and ρ_a^0 is the value of the asthenospheric density at the base of the lithosphere.

Many constitutive laws can be tested to model the behaviour of the plates. For the sake of simplicity elastic and elastoplastic rheologies were used in this work but the results presented therein concern only the case of elastoplastic plates. The use of such a rheology is supported by the fact that we neglected the lower part of the lithosphere assuming that its mechanical resistance is too low to transmit any significant tectonic stresses. Thus the thickness of the plate

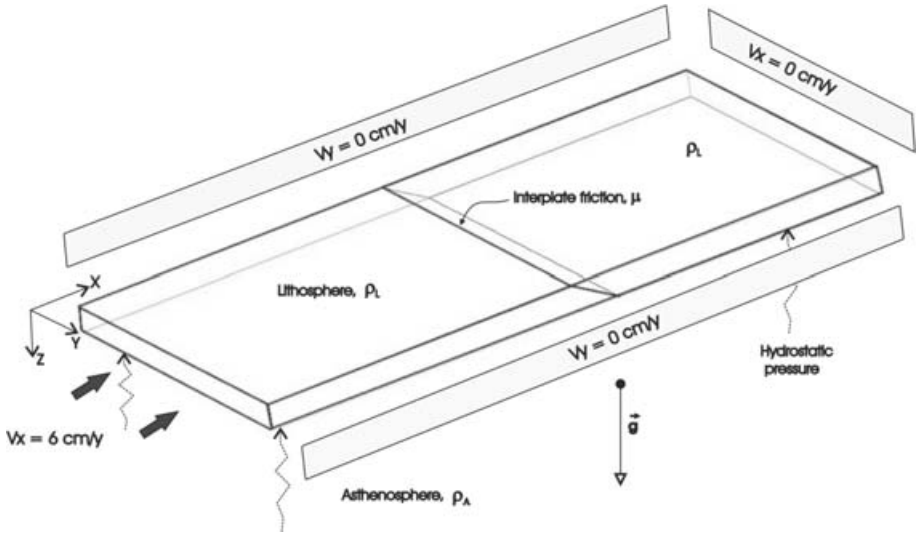

Figure 1. Boundary conditions of the 3-D models. The lithosphere is underlain by an inviscid asthenospheric fluid. Both the lithosphere and the asthenosphere are characterized by specific densities (ρ_L and ρ_A, respectively). The asthenosphere acts at the base of the lithosphere through a hydrostatic pressure. The subduction plane is defined by a friction coefficient, μ. The whole model is loaded by body forces, $\vec{g}$. The upper surface is a free surface. A horizontal velocity is applied at the downgoing plate boundary. The model is 1000 km long, 500 km wide and 40 km thick.

Table 1. Mechanical parameters used for the simulations.

Parameters	Values
Young modulus, E	10^{11} Pa
Poisson ratio, ν	0.25
Cohesion, c	10 MPa
Friction angle, ϕ	15°
Lithosphere density, ρ_l	3100–3300 kg m^{-3}
Asthenosphere density, ρ_a	3200 kg m^{-3}
Effective friction coefficient, μ	0–0.2

used in this model represents the equivalent mechanical thickness of the lithosphere limited in depth by the 600 °C isotherm (Turcotte & Schubert 1982) and it is not its actual thickness. Therefore the thickness is fixed to 40 km which approximately corresponds to a 80 Ma oceanic plate (e.g. Kirby 1983).

In the elastic domain the constitutive law is simply given by

$$\mathcal{M}(\boldsymbol{\sigma}, \boldsymbol{d}) = 2G\boldsymbol{d} + \lambda \mathrm{tr}(\boldsymbol{d})\, \mathbf{I}, \tag{4}$$

where λ and G are the Lamé parameters, $\mathbf{I}$ is the identity tensor and tr the trace operator. Typical values for the lithosphere are chosen for associated Young's modulus (10^{11} Pa) and for Poisson's ratio (0.25).

In order to mimic a pressure dependent yield strength we use the elastoplastic Drucker–Prager model (Desai & Siriwardane 1984) for which the yield function is given by

$$F(\boldsymbol{\sigma}) = J_2(\boldsymbol{\sigma}) + \alpha I_1(\boldsymbol{\sigma}) - \alpha P_0 \leq 0, \tag{5}$$

where $J_2(\boldsymbol{\sigma}) = \sqrt{3/2}\sqrt{(\sigma_1-\sigma_2)^2+(\sigma_2-\sigma_3)^2+(\sigma 3-\sigma 1)^2}$ is the second invariant of the deviatoric part of the stress tensor, $I_1(\boldsymbol{\sigma}) = (\sigma_1+\sigma_2+\sigma_3)/3$ is the isotropic part, $\alpha = 6\sin(\phi)/(3-\sin(\phi))$ and $P_0 = c/\tan(\phi)$ with c the cohesion and ϕ the friction angle. The materials parameters used in this study are listed in Table 1.

2.3 Numerical aspects

An approximated solution of the problem (1)–(2) is computed by the numerical code ADELI which has been used in many geodynamic applications either in 2-D context or in 3-D ones. This code use the finite elements method for the spatial discretization and an explicit finite difference scheme for the time discretization based on the dynamic relaxation method (e.g. Underwood 1983; Cundall & Board 1988). More details about previous versions of this code can be found in Hassani *et al.* (1997) and in Chéry *et al.* (2001). The current version uses an external tetrahedral mesh generator, the GMSH tool (Geuzaine & Remacle 2004), which allows us to mesh any given body. The surface boundaries are then constituted with triangular facets and a special processing in the computation of surface forces is needed at each time step for those facets which progressively go into the asthenosphere. The contribution of an entirely immersed facet, $\mathcal{T}$, to the equivalent nodal forces at node i of $\mathcal{T}$ is classically given by

$$\boldsymbol{F}_i = -\int_{\mathcal{T}} P_a \phi_i \boldsymbol{n}\, \mathrm{d}S, \tag{6}$$

where $\phi_i(\boldsymbol{x})$ is the finite element basis function attached to the node i and $\boldsymbol{n}$ is the outward unit normal. Using the finite element approximation on the triangular facet $P_a \approx \sum_j P_a^j \phi_j$ where P_a^j is the pressure at the node j of the facet, the integral in (6) can be explicitly computed for three-noded linear triangle. Now, if the facet is partially immersed in the asthenosphere, the integral is taken only over the immersed area $\mathcal{T}_{im} \subseteq \mathcal{T}$ for which the geometry must be first determined. For this purpose we proceed as follows: the polygonal line L corresponding to the lower contact between the overriding plate and the slab is first determined and the intersection between the facet $\mathcal{T}$ and L is checked. If $\mathcal{T} \cap L$ is a segment, $\mathcal{T}_{im}$ is a triangular or a quadrangular area. In the first case, the computation of the nodal forces $\boldsymbol{F}_i$ follows the same way as in the immersed case while in the second case we define $\mathcal{T}_{em}$ as the complementary triangular area and use the formula $\int_{\mathcal{T}_{im}} = \int_{\mathcal{T}} - \int_{\mathcal{T}_{em}}$ to bring back all integral over triangular zones. If $l = \mathcal{T} \cap L$ is a polygonal line we approximate it by simply joining the two points of l that are on the boundary of $\mathcal{T}$.

Several tests were performed to check the numerical accuracy of the results and a mesh resolution of 95 000 elements with an element size of 11 and 12 km, was finally used for the simulations.

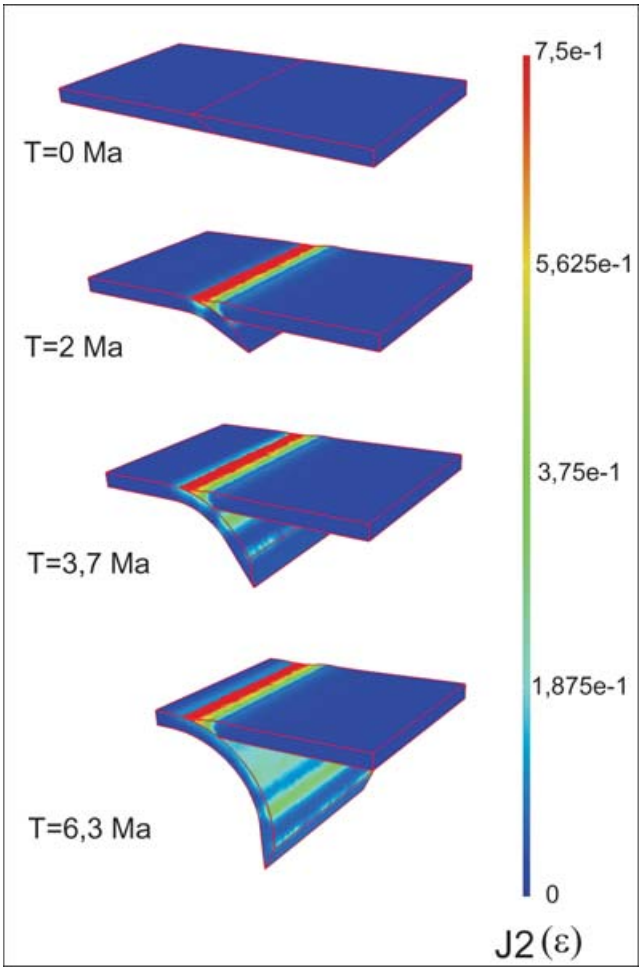

Figure 2. Time evolution of the reference case showing the second invariant of the deviatoric strain tensor. An elastoplastic rheology is used with $\Delta\rho = 0$ and $\mu = 0$. The results are plotted with the Medit visualization software (Frey 2001).

3 3-D ORTHOGONAL CONVERGENCE

The first set of 3-D experiments corresponds to the reference geometry, in which the margin is linear and is subjected to an orthogonal convergence (Fig. 1). With the presented results we show the major effects of two fundamental parameters, the density contrast between the lithosphere and the asthenosphere ($\Delta\rho = \rho_l - \rho_a$) and the interplate friction coefficient, on the shallow slab geometry and the topography and the stress in the plate. These 3-D experiments are similar to the 2-D experiments of Hassani *et al.* (1997).

The Fig. 2 presents the time evolution of the deformation intensity in the reference case, which is characterized by $\Delta\rho = 0$ and $\mu = 0$. The figure shows that for an elastoplastic slab, a great part of the bending deformation acquired during subduction initiation is permanent and remains within the upper part of the subducting plate. This causes the slab to roll up and gives rise to significant curvature of the plate in the upper mantle inducing the rolling up of the slab. In contrast, an elastic rheology makes the slab to subduct regularly with the initial dip of 30°.

3.1 Effects of the density contrast

The lateral variations of the age of the seafloor and/or the nature of the subducting plate (oceanic asperities like seamounts, plateaus, island arcs, etc.) modify the slab pull force and influence the behaviour of the slab. As previously observed by Shemenda (1993, 1994), variations of the density contrast enhance significant changes in the slab geometry and in the deformation pattern within the upper plate. For a negative density contrast (the slab is lighter than the asthenosphere) (Fig. 3a), the slab subducts and when a sufficient length is reached, the resulting bending moment, which increases with the slab length, leads to the underplating of the slab beneath the overriding plate. On the contrary, a positive density contrast (the slab is denser than the asthenosphere) (Fig. 3b) induces the sinking of the slab which tends to become vertical. Specific topographies of the upper plate are dependent on the variations of density contrast and slab geometry, which affect the interplate pressure applied on the subduction plane. We observe that regardless of the density contrast between the lithosphere and the asthenosphere, there is no strain propagation landward and strain is always restricted to the arc area.

3.2 Effects of the interplate friction

The interplate friction is also a fundamental parameter in the evolution of a subduction zone, since it controls the plate coupling and induces an increase of the compressive component in the overriding plate. In nature, a strong interplate coupling is likely associated with tectonic erosion that is enhanced, for instance, by topographic irregularities at the top of the subducting plate. On the contrary, a low coupling is preferentially associated with sedimentary accretion

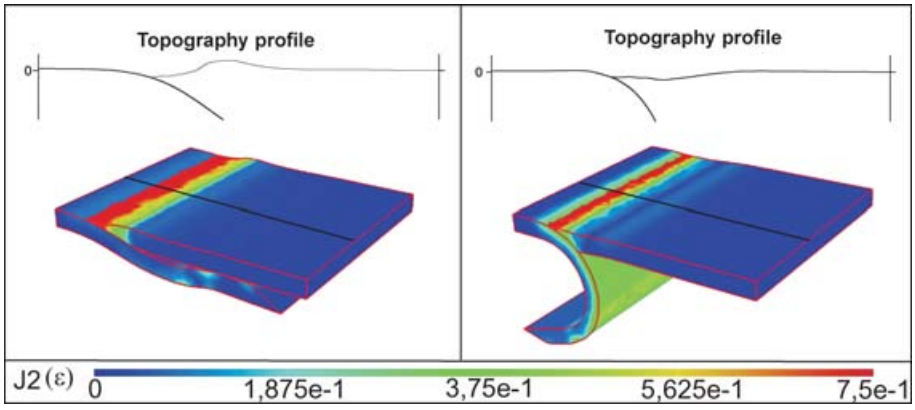

Figure 3. Effects of the density contrast on the slab behaviour and the upper plate deformation for T = 6.3 Ma. An elastoplastic rheology is used for both models. (a) $\Delta\rho = -100\ \mathrm{kg\,m^{-3}}$ and $\mu = 0$; (b) $\Delta\rho = 100\ \mathrm{kg\,m^{-3}}$ and $\mu = 0$.

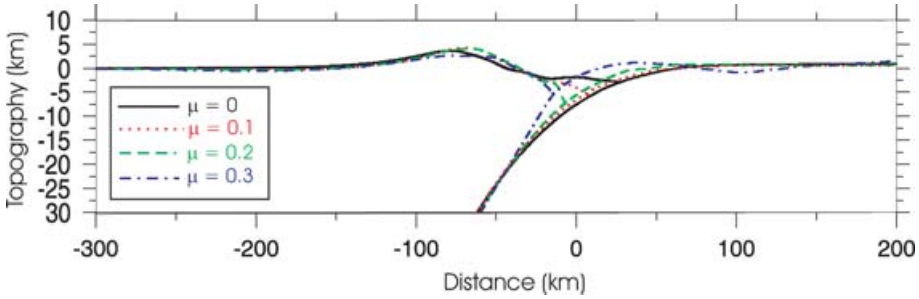

Figure 4. Effects of the friction coefficient on the upper plate topography for $T = 6.3$ Ma. These simulations were performed with an elastoplastic model using $\Delta\rho = 0$ and friction coefficients range from $\mu = 0$ to 0.3.

along the margin. However, recent studies showed that the interplate coupling may vary drastically due to the structure of the subduction channel, which may locally induce a strong fluid overpressure along the interplate contact and favour the subduction erosion process (Sage *et al.* 2006).

Fig. 4 displays the topography profiles from elastoplastic models with a $\Delta\rho = 0$ and interplate friction μ ranging from 0 to 0.3. The fact that many processes such as erosion, thermal effect lithosphere rheology and lithosphere–asthenosphere coupling are not accounted for in our modelling, may explain the unrealistic topography of the upper plate. First, we see that if no interplate friction is applied along the subduction plane, the resulting margin topography is quite smooth and a highly deformed area develops in a localized region within the margin. On the contrary, with higher friction, the margin exhibits a very steep slope and the deformation is not restricted to the margin but appears to be pervasive into the upper plate. In nature subduction zones with a high plate-slab coupling, which is revealed by high magnitude earthquakes, are mainly recorded along the Andean margin. The upper plate in these regions is subjected to a large compressional regime characterized by fold-and-thrust belts and margin topography with steep slopes. In contrast, subduction zones with a very low interplate coupling (lower magnitude seismicity) in the SW Pacific ocean are mainly characterized by an extensional regime in the upper plate (Pacheco *et al.* 1993; Scholz & Campos 1995; Conrad *et al.* 2004). For very high values of the friction coefficient ($\mu = 0.3$), our models show that the subduction is inhibited. We also observe that all of the compression is first accommodated by the buckling of the slab and then by the transmission of this compression to the upper plate (Fig. 5). A similar phenomenon is observed in the Indian Ocean where a large wave length undulation of the seafloor occurs due to the locking of the Himalayan collision (Neprochnov *et al.* 1988; Krishna *et al.* 1998). The models presented in this work show that the evolution of the upper plate topography is intimately linked to the compressive component transmitted from the slab. Steep topography reveals a strong compressive stress transmitted to the upper plate, whereas smooth topography is associated with weak coupling and an extensional stress regime. Thus topographic observations could be a good indicator of the intensity of the interplate coupling.

4 CURVED MARGIN GEOMETRIES

In comparison to the reference case, we performed some simulations with convex and concave margins to analyse the stress regime induced by such geometries. The initial model is displayed in Fig. 6. To avoid boundary conditions effects, a linear segment is placed on each side of the curved area that ensures a free evolution of the mesh elements in the convexity. We present the results for $\Delta\rho = 0$ and $\mu = 0$ in both geometries. A range of density contrasts ($\Delta\rho = \pm 100$ kg m^{-3}), interplate friction coefficients ($\mu = 0 - 0.3$) and values of margin curvature ($r = 160$, 283 and 400 km) were tested to determine their respective effect on the upper plate deformation. The curvature values were defined at the Earth's surface, since most of the arcs and trenchs can be fit by the arc of a circle (see Fig. 6 for more details). In our examples the radius values $r = 160$, 283 and 400 km could be compared to the Marianas, the Aleutian and the Ryukyu subduction zones, respectively. As noted by Jarrard (1986), these determinations are subjective, since some regions like Kurile-Kamchatka or Aleutian-Alaska may be defined by a single long arc or by several portions of smaller arcs. Moreover, these curvature values are viewed in a Cartesian geometry and would be consequently reduced but not entirely balanced in considering the Earth sphericity.

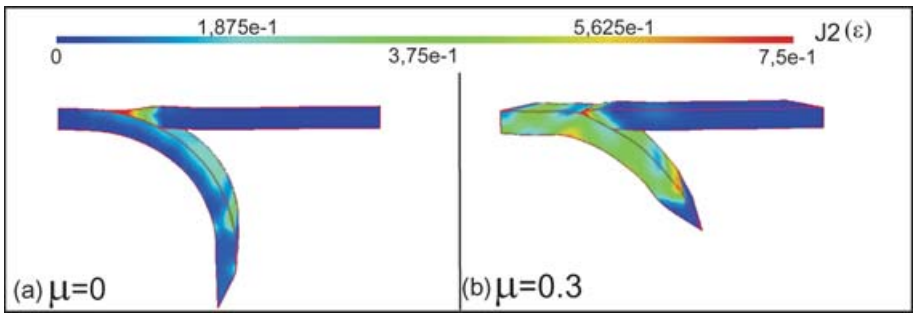

Figure 5. Effect of a strong friction coefficient ($\mu = 0.3$) on the plates deformation for $T = 6.3$ Ma. An increase of the interplate friction leads to an increase of the internal deformation of the subducting plate up to the buckling of the slab's trailing plate (b). This result can be compared to the reference model in Fig. 2 performed with $\mu = 0$.

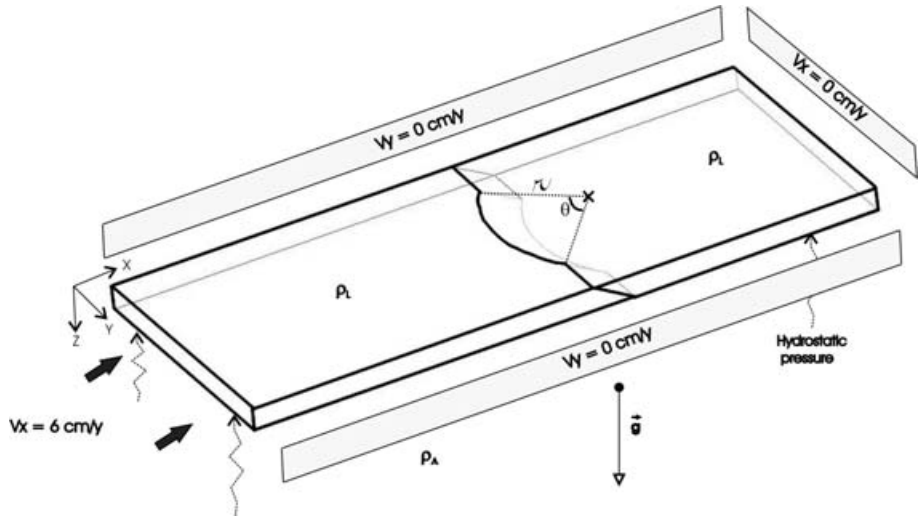

Figure 6. Initial geometry for a convex model. In the model, the arcuate arc shape is amplified through a decrease of the radius value. This value is determined from the ratio between the length of the circle chord and the maximum distance between the chord and the arc of circle. The boundary conditions are similar to those used in the reference model.

In the computations, the convergence is orthogonal to the linear boundaries.

4.1 Effects of the curvature

Fig. 7 shows the results obtained for $\Delta\rho = 0$, $\mu = 0$ and $r = 283$ km. Compared to the reference case ($r = \infty$), a geometric discontinuity in the margin induces an irregular strain pattern within the upper plate (Figs 7a and d). In the convex margin model (Figs 7a–c), the highest strain is mainly localized in the convex area, which is characterized by the highest topography. On the contrary, the front of the concave zone (Figs 7d–f) is represented by a subsident region surrounded by two uplifted zones, due to their approximated convex shape. These specific topography patterns are related to the dip direction of the interplate contact, since in the presented results the interplate pressure is always parallel to the trench normal component. Thus a convex boundary will imply convergent stresses in the upper plate, while divergent stresses will be induced for a concave boundary. The effect of such a mechanism on the topography can be significant, since the Fig. 8 shows that for the smallest convex curvature we modelled ($r = 283$ km), the topography in the convex area can be twice as high as in the reference linear case. Fig. 8 also shows that whatever the curvature value, a convexity always induces compression and uplift of the margin, whereas a concavity is related to extension and subsident margin. This upper plate behaviour is likely related to the slab dip at the plate interface (Fig. 8), which is shallower along a convex margin than along a linear margin and steeper along a concave margin.

4.2 Effects of the density

For the linear reference case, we observed that a positive density contrast ($\Delta\rho = 100$ kg m^{-3}, and $\mu = 0$) induces the formation of a forearc basin due to the hydrostatic suction along the interplate contact (Hassani *et al.* 1997) (Fig. 3b). With a convex geometry, this strong forearc subsidence is only observed on each side of the convex area, corresponding to the linear boundaries (Fig. 6), where the lateral forearc basins reach up to 10 km in depth. An extensional stress regime prevail in the upper plate behind the two linear margins (Fig. 7). With a positive density contrast, the convex arc zone is still characterized by significant uplift (4.3 km high) (Fig. 9a) and compressional stresses. In the same way, a concave model with a negative density contrast induces a forearc basin in front of the concavity. This forearc basin is amplified with positive density contrast and reaches up to 12 km in depth in our models (Fig. 9b). It induces a strong extensional regime landward, while the two lateral areas similar to convex margins record an uplift.

We conclude that a curved margin ($r = 283$ km) is less sensitive than a linear margin to the variation of $\Delta\rho$ (Figs 3 and 9). For the range of values we simulated, the curvature parameter seems to have a stronger effect on stress regime within the upper plate than density contrast.

4.3 Effects of the interplate friction

An interplate friction coefficient makes the strain more pervasive into the overriding plate and reduces the margin convexity due to the higher compressive stress transmitted to the upper plate (Fig. 10). The deformation is mainly located within the curved area (Fig. 10b) and it may be considered as preferential zones for initiation of strike-slip faults McCaffrey & Nabelek (1998), since this area is subjected to an extensional stress field in the *y*-axis direction (Fig. 11b).

An increase of the interplate friction also produces some important variations of the stress regime within the shallow slab (Fig. 11). High interplate friction coefficient leads to a stronger flexure of the slab, which tends to bend around the convex margin. This bending is underlined by a compressive regime localized along the convex margin in surface and parallel to the interplate plane downward (cross-section in Fig. 11b). However, an extensional area in the *y*-axis direction is clearly identified between this compressive area and the interplate plane. This observation indicates that a lateral escape of the upper part of the slab is induced by the convexity and a strong interplate coupling. This behaviour is amplified with an increase of the margin curvature. These results are in good agreement with those obtained by Boutelier (2004), who suggested that this extensional phase could support the rock exhumation along convex margins.

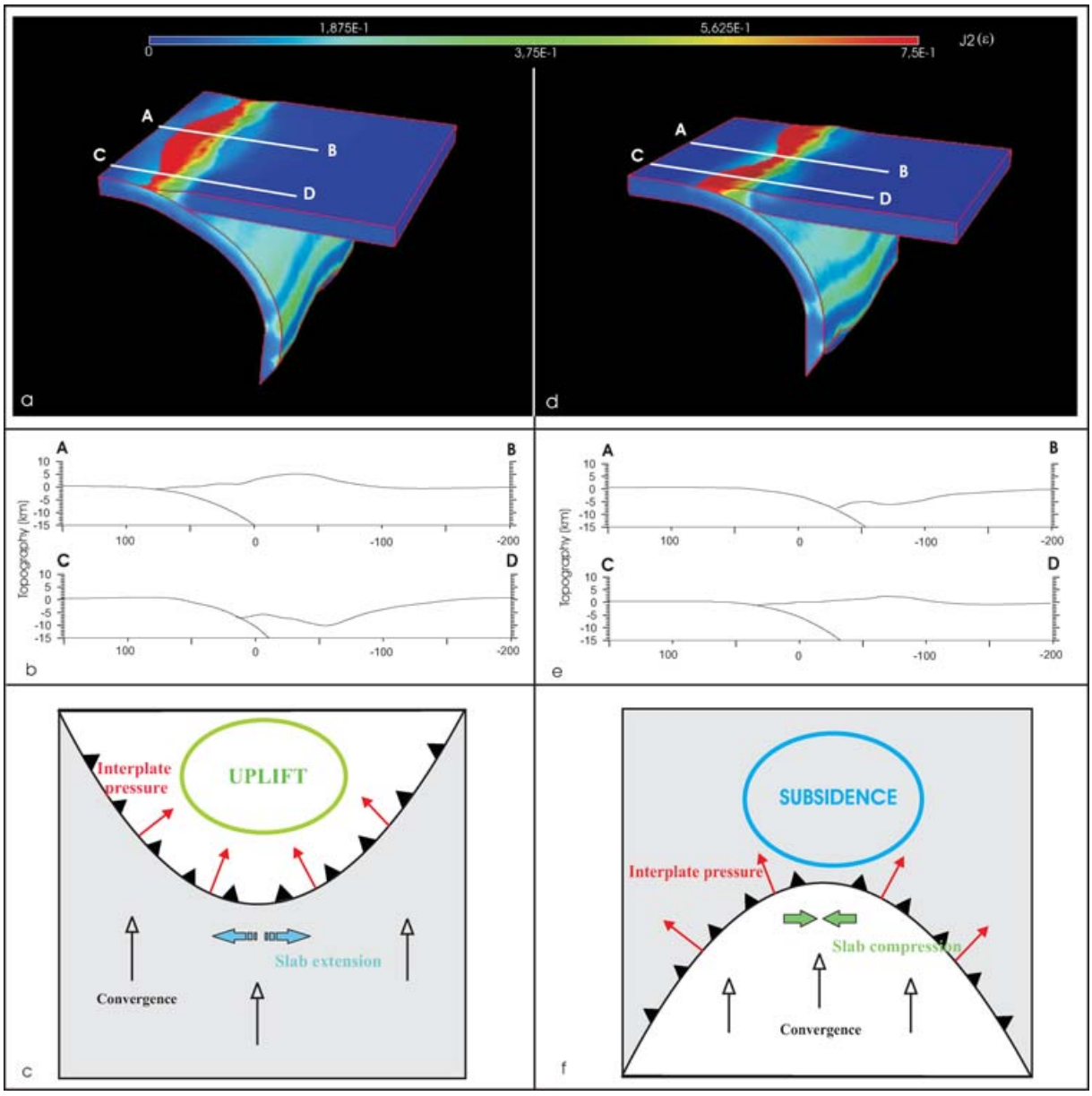

Figure 7. (a) and (d) strain pattern for convex and concave geometry using $\Delta\rho = 0$ and $\mu = 0$. The convex area is defined by the highest topography, while the concave area is subjected to a strong subsidence. (b) and (e) Comparison between the topography profiles obtained for a convex and a concave model; (c) and (f) Schematic representation of the mechanism responsible for this deformation pattern. These models were perform with $r = 283$ km. $T = 6.3$ Ma. (c and f modified from Boutelier 2004).

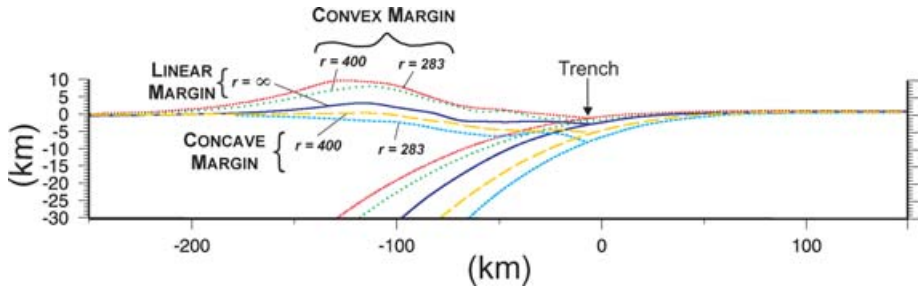

Figure 8. Topography profiles obtained for different values ($r = 283$ km, 400 km and ∞) and types of curvature (concave to convex shape).

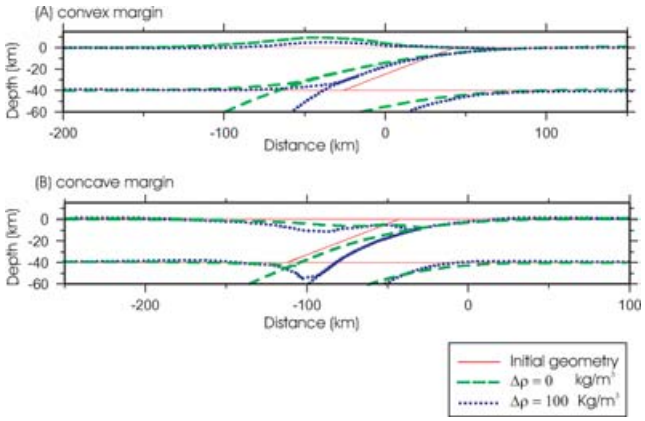

Figure 9. The cross-sections are built at the end of the computation in the middle of the models (see cross-section a–b in Fig. 7). For a zero interplate friction, the curvature parameter seems to control the stress regime and the resulting topography.

5 DISCUSSION

With the numerical setup used in this study, the results show that for a linear margin, extensional or compressional tectonic regime within the upper plate is obtained depending on the density and the interplate friction coefficient parameters. The introduction of a margin curvature appears to mainly control the tectonic regime, since an oceanward convex shape induces a margin uplift related to the compression regime. In contrast, the margin in front of an oceanward concave margin undergoes a subsidence and induces an extensional regime in the upper plate. Moreover, this convex/compression and concave/extension association is observed regardless of the magnitude of curvature. These results are similar to those obtained by Boutelier (2004), despite their different setup. Thus, a slight change in the margin geometry from convex to linear or even concave geometry would induce a significant variation of the stress regime within the upper plate.

However, the comparison between our results with field observations cannot be attempted directly, since we didn't take into account mantle flow effects on lithosphere evolution. For instance, the results display unrealistically high values of topography that may be explained by the absence of a full lithosphere–asthenosphere coupling. Furthermore, a significant fraction of the topography was shown to be dynamically controlled by the lithosphere–asthenosphere interactions (Billen *et al.* 2003; Husson 2006). These calculations reasonably reproduce observed topography without including a realistic elasto-viscoplastic rheology for the lithosphere.

Nonetheless, some important results arise from this study, and they require particular attention in comparison to the field observations. The best example of an oceanward concave margin is the Bolivian Orocline in South America. The comparison of this natural analogue with our results is a bit ambiguous because the Bolivian Orocline, which is one of the largest mountain ranges, is lying in a predicted extensional area. Interpretations of data from several workers suggest that crustal shortening alone can not account for the total thickening of the region (Allmendinger *et al.* 1997; Rochat *et al.* 1999; Gregory-Wodzicki 2000). The Altiplano is indeed made of an anomalously large amount of magmatic intrusions that may contribute to a large fraction of the crustal thickening. The analysis of the slab dip evolution through time and the variations of the convergence rates suggest that the extented magmatic episodes would be likely related to extensional tectonics in the forearc and arc areas during the initial stage of the Central Andes build-up (Jordan *et al.* 2001) (T. Sempere, personal communication 2007). The numerical results presented in this work give new insights about this interpretation, since they show that the concave shape of the andean margin can trigger such an extensional regime.

Oceanward convex margins, which are the most common geometries, can be likely illustrated by the Marianas subduction zone. Contrary to our results that predict a compression within a convex upper plate, a well-established backarc basin is observed behind the Marianas volcanic arc. Husson (2006) showed that the resulting dynamic topography was likely explained by the subduction-induced stresses of the underlying viscous mantle, which suggests that a backarc basins are mainly controlled by the mantle flow (Sdrolias & Muller 2006). However, Stern & Smoot (1998) noted a regional uplift in the arc and forearc zones localized in the southern convex part of the Marianas that is subjected to an orthogonal convergence. This local feature is not predicted by the dynamic topography models, but instead is in good agreement with our results. Thus, like in the Central Andes region, this correlation would likely reflect the importance of modelling the third direction to explain some punctual variations of the tectonic regime.

Finally, we can also attempt to compare the results to the initial stages of the backarc basin opening. The location of an arc rupture can vary in subduction zones (Hawkins *et al.* 1984). For example, the

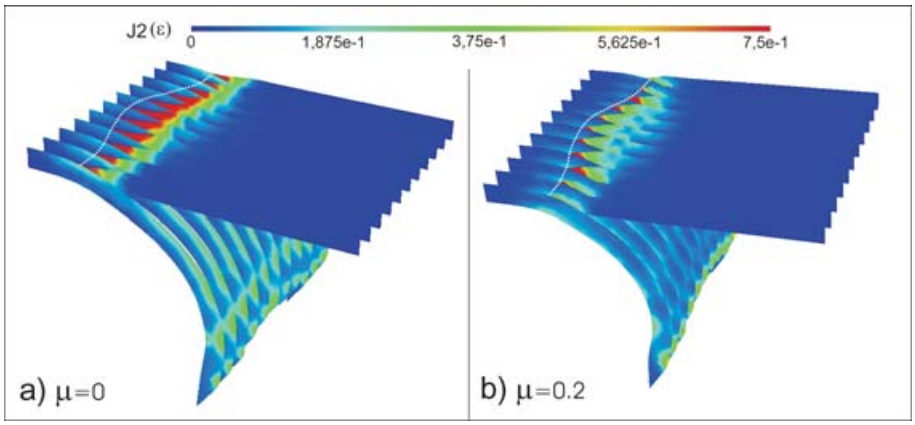

Figure 10. Comparison in cross-section of convex models obtained for $\Delta\rho = 0$. (a) $\mu = 0$ and (b) $\mu = 0.2$. Note that the strong penetrative deformation is mainly localized into the convex area. These results are obtained at the end of the simulation.

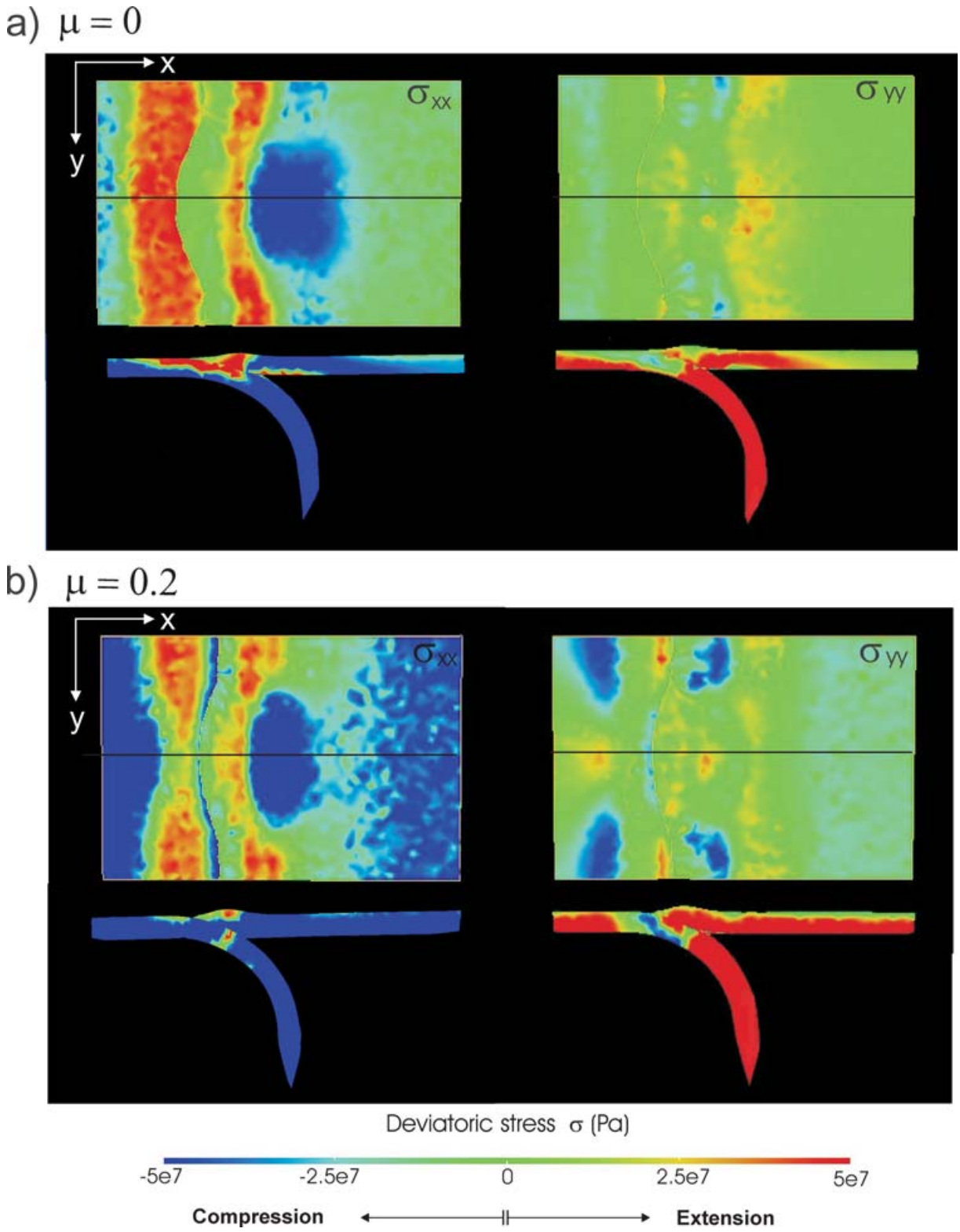

Figure 11. Comparison of the horizontal deviatoric stress σ_{xx} and σ_{yy} for a convex margin geometry ($\Delta\rho = 0$ and $r = 283$ km): (a) interplate friction coefficient $\mu = 0$; (b) interplate friction coefficient $\mu = 0.2$. See the text for discussion.

mostly linear Palau-Kyushu ridge split on its 'backarc side' (Okino *et al.* 1998; Okino *et al.* 1999), while the Mariana arc rifted on its 'forearc side', which isolated most of the initial arc in the current remnant ridge (Bloomer *et al.* 1989). A similar phenomenon occured in the Tonga subduction zone where the old Tonga volcanic arc from 15°S to 18°30′S forms part of the Lau remnant ridge that separated from the current active Tofua volcanic arc. This observation suggests that the Lau backarc basin initiated also in the forearc

domain (Hawkins *et al.* 1984; Bonnardot *et al.* 2007). The Marianas and Tonga subduction zones have a common point related to the subduction of a significant bathymetric feature, the Osagawa plateau and the Louisville Seamount Chain, respectively. The collision between a seamount and the margin generates an oceanward concave margin that results in a forearc basin (Collot & Fischer 1989). We show in this study that a slight change in the margin geometry might modify the stress regime within the upper plate. Thus, together with the landward migration of the overriding plate (Sdrolias & Muller 2006), the geometrical consequences induced by a ridge subduction could act as a precursor to preferentially split the volcanic arc in the forearc side. Once the backarc extension is established, the global mantle flow dynamic would control the evolution of the regional system.

6 CONCLUSION

In conclusion, the 3-D ADELI numerical code is an appropriate tool for studying the effects of the plate-plate coupling on the lithospheric deformation in subduction zone and does allow the resolution of some local strain pattern variations unexplained by global mantle dynamics processes.

We showed in this work that an oceanward convex margin induces a compressive stress regime in the upper plate, which is uplifted. On the contrary, an oceanward concave margin is subjected to an extensional stress regime resulting in the formation of a forearc basin. For the range of parameters we used, such a behaviour was independent of the contrast of density between the lithosphere and the asthenosphere and to the interplate friction coefficient. Thus, this study supports the fact that the third dimension is fundamental when dealing with lithospheric deformations. Future work might attempt to quantify the strain partitioning associated with oblique convergence and oceanic asperities subduction, since various 3-D geometries for both the overriding and subducting plates can now be taken into account with this numerical code.

ACKNOWLEDGMENTS

We are grateful to Rob Govers, Erik Kneller and anonymous reviewer for constructive comments and a careful check of the English grammar, which greatly help to improve this manuscript.

REFERENCES

Allmendinger, R., Jordan, T., Kay, S. & Isacks, B., 1997. The evolution of the Altiplano-Puna plateau of the Central Andes, *Ann. Rev. Earth planet. Sci.,* **25,** 139–174.

Arcay, D., Tric, E. & Doin, M.-P., 2005. Numerical simulations of subduction zones - Effect of slab dehydration on the mantle wedge dynamics, *Phys. Earth planet. Inter.,* **149,** 133–153.

Billen, M.I., Gurnis, M. & Simons, M., 2003. Multiscale dynamics of the Tonga-Kermadec subduction zone, *Geophys. J. Int.,* **153,** 359–388.

Bloomer, S.H., Stern, J.R. & Smoot, N.C., 1989. Physical volcanology of the submarine Mariana and Volcano arcs, *Bull. Volcanol.,* **51,** 210–224.

Bonnardot, M.-A., Régnier, M., Ruellan, E., Christova, C. & Tric, E., 2007. Seismicity and state of stress within the overriding plate of the Tonga-Kermadec subduction, zone, *Tectonics,* **26,** TC 5017, doi:10.1029/2006TC002044.

Bonnardot, M.-A., Hassani, R. & Tric, E., submitted. Numerical modelling of lithosphere-asthenosphere interaction in a subduction zone.

Boutelier, D., 2004. La modélisation expérimentale tridimensionnelle thermomécanique de la subduction continentale et l'exhumation des roches de ultra-haute pression/basse température, *PhD thesis*, Université Nice–Sophia Antipolis.

Buiter, S., 2000. Surface deformation resulting from subduction and slab detachment, *PhD thesis*, University of Utrecht, Netherlands.

Cadek, O. & Fleitout, L., 2003. Effect of lateral viscosity variations in the top 300 km on the geoid and dynamic topography, *Geophys. J. Int.,* **152,** 566–580.

Chéry, J., M., Z. & Hassani, R., 2001. An integrated mechanical model of San Andreas fault in central and northern California, *J. geophys. Res.,* **106**(B10), 22 051–22 066.

Collot, J.-Y. & Fischer, M.A., 1989. Formation of forearc basins by collision between seamounts and accretionary wedges: an example from the New Hebrides subduction zone, *Geology,* **17,** 930–933.

Conrad, C., Bilek, S. & Lithgow-Bertelloni, C., 2004. Great earthquakes and slab pull: interaction between seismic coupling and plate-slab coupling, *Earth. planet. Sci. Lett.,* **218,** 109–122.

Cundall, P. & Board, M., 1988. A microcomputer program for modeling large strain plasticity problems, in *Numerical Methods in Geomechanics*, pp. 2101–2108, ed. Swoboda, C., Balkema, Rotterdam.

De Franco, R., Govers, R. & Wortel, R., 2006. Numerical comparison of different convergent plate contacts: subduction channel and subduction fault, *Geophys. J. Int.,* **171,** 435–450.

Desai, C. & Siriwardane, H., 1984. *Constitutive Laws for Engineering Materials With Emphasis on Geologic Materials*, p. 457, Prentice-Hall, Englewood Cliffs, NJ.

Faccenna, C., Heuret, A., Funiciello, F. & Lallemand, S., 2007. Predicting trench and plate motion from the dynamics of a strong slab, *Earth planet. Sci. Lett.,* **257,** 29–36.

Frank, F.C., 1968. Curvature of island arcs, *Nature,* **220,** 363.

Frey, P.J., 2001. Medit, an interactive mesh visualization software (Release 2.3), RT-INRIA 0253, http://www.ann.jussieu.fr/∼frey/logiciels/medit.html.

Funiciello, F., Faccenna, C., Giardini, D. & Regenauer-Lieb, K., 2003. Dynamics of retreating slabs. 2: insights from three-dimensional laboratory experiments, *J. geophys. Res.,* **108**(B4), 2207, doi:10.1029/2001JB000896.

Gardi, A., Sabadini, R., Ferraro, C. & Aoudia, A., 2003. The interplay between global tectonic processes and the seismic cycle in the Umbria-Marche seismogenic region, *Geophys. J. Int.,* **155,** 1093–1104.

Geuzaine, C. & Remacle, J.-F., 2004. Gmsh, a mesh generator (Release 1.56.2), http://www.geuz.org/gmsh/.

Govers, R. & Wortel, M., 2005. Lithosphere tearing at STEP faults: response to edges of subduction zones, *Earth planet. Sci. Lett.,* **236,** 505–523.

Gregory-Wodzicki, K., 2000. Uplift history of the Central and Northern Andes: a review, *G.S.A. Bull.,* **112,** 1091–1105.

Hager, B.H. & O'Connell, R.J., 1978. Subduction zone dip angles and flow driven by plate motion, *Tectonophysics,* **50,** 111–133.

Hager, B.H. & O'Connell, R.J., 1979. Kinematic models of large-scale flow in the Earth's mantle, *J. geophys. Res.,* **84,** 1031–1048.

Hassani, R., Jongmans, D. & Chery, J., 1997. Study of plate deformation ans stress in subduction processes using two-dimensional numerical models, *J. geophys. Res.,* **102**(B8), 17 951–17 965.

Hawkins, J.W., Bloomer, S.H., Evans, C.A. & Melchior, J.T., 1984. Evolution of intra-oceanic arc-trench systems, *Tectonophysics,* **102,** 175–205.

Heuret, A. & Lallemand, S., 2005. Plate motions, slab dynamics and back-arc deformation, *Phys. Earth planet. Int.,* **149,** 31–51.

Husson, L., 2006. Dynamic topography above retreating subduction zones, *Geophys. Res. Lett.,* **34,** 741–744.

Jarrard, R.D., 1986. Relations among subduction parameters, *Rev. Geophys.,* **24**(2), 217–284.

Jean, M. & Touzot, G., 1988. Implementation of unilateral contact and dry friction in computer codes dealing with large deformation problems, *J. Th. Appl. Mech., spec. issue,* **1,7**.

Jordan, T., Burns, W., Veiga, R., Pangaro, F., Copeland, P., Kelley, S. & Mpodozis, C., 2001. Extension and basin formation in thesouthern Andes

caused by increased convergence rate: a mid-Cenozoic trigger for the Andes, *Tectonics,* **20**(3), 308–324.

Kirby, S.H., 1983. Rheology of the lithosphere, *Rev. Geophys. Space Phys.,* **21**(6), 1458–1487.

Krishna, K.S., Ramana, V., Rao, D.G., Murthy, K.S.R., Rao, M.M.M., Subrahmanyam, V. & Sarma, K.V.L.N.S., 1998. Periodic deformation of oceanic crust in the central Indian Ocean, *J. geophys. Res.,* **103**(B8), 17 859–17 875.

Lallemand, S., Heuret, A. & Boutelier, D., 2005. On the relationships between slab dip, back-arc stress, upper plate absolute motion, and crustal natures in subduction zones, *Geochem. Geophys. Geosyst.,* **6**(9), doi:10.1029/2005GC000917.

Mandel, J., 1966. *Mécanique des milieux continus*, Gauthier-Villars, Paris.

Manea, V. & Gurnis, M., 2007. Subduction zone evolution and low viscosity wedges and channels, *Earth planet. Sci. Lett.,* **8887,** doi:10.1016/j.epsl.2007.08.03.

Mantovani, E., Viti, M., Babbucci, D., Tamburelli, C. & Albarello, D., 2001. Back-arc extension: which driving mechanism?, *J. Virtual Explor.,* **3,** 17–45.

Marsden, J. & Hughes, T., 1983. *Mathematical Foundations of Elasticity*, Prentice-Hall Inc., Englewood Cliffs.

McCaffrey, R. & Nabelek, J., 1998. Role of oblique convergence in the active deformation of the Hymalayas and southern Tibet plateau, *Geology,* **26**(8), 691–694.

Morra, G. & Regenauer-Lieb, K., 2006. A coupled solid-fluid method for modelling subduction, *Philos. Mag.,* **86**(21–22), 3307–3323.

Morra, G., Regenauer-Lieb, K. & Giardini, D., 2006. Curvature of oceanic arcs, *Geology,* **34**(10), 877–880.

Neprochnov, Y.P., Levchenko, O.V., Merklin, L.R. & Sedov, V.V., 1988. The structure and tectonics of the intraplate deformation area in the Indian Ocean, *Tectonophysics,* **156,** 89–106.

Noll, W., 1972. A new mathematical theory of simple materials, *Arch. Rat. Mech. Anal.,* **48,** 1–50.

Okino, K., Kasuga, S. & Ohara, Y., 1998. A new scenario of the Parece Vela Basin genesis, *Mar. Geophys. Res.,* **20,** 21–40.

Okino, K., Ohara, Y., Kasuga, S. & Kato, Y., 1999. The Philippine Sea: new survey results reveal the structure and the history of the marginal basins, *Geophys. Res. Lett.,* **26,** 2287–2290.

Pacheco, J.F., Sykes, L.R. & Scholz, C.H., 1993. Nature of the seismic coupling along simple plate boundaries of the subduction type, *J. geophys. Res.,* **98**(B8), 14 133–14 159.

Piromallo, C., Becker, T., Funiciello, F. & Faccenna, C., 2006. Three-dimensional instantaneous mantle flow induced by subduction, *Geophys. Res. Lett.,* **33**(L08304), doi:10.1029/2005GL025390.

Rochat, P., Herail, G., Baby, P. & Mascle, G., 1999. Crustal balance and control of the erosive and sedimentary processes on the Altiplano formation, *C. R. Acad. Sci. Paris,* **328,** 189–195.

Royden, L. & Husson, L., 2006. Trench motion, slab geometry and viscous stresses in subduction systems, *Geophys. J. Int.,* **167,** 881–905.

Sage, F., Collot, J.-Y. & Ranero, C., 2006. Interplate patchiness and subduction-erosion mechanisms: evidence from depth-migrated seismic images at the central Ecuador convergent margin, *Geology,* **34,** 997–1000.

Schellart, W., 2005. Influence of the subducting plate velocity on the geometry of the slab and migration of the subducting hinge., *Earth planet. Sci. Lett.,* **231,** 197–219.

Schellart, W. & Lister, G., 2004. Tectonic models for the formation of arc-shaped convergent zones and backarc basins, in *Orogenic curvature: Integrating Paleomagnetic and Structural Analyses*, pp. 237–258, eds Sussman, A. & Weil, A., Geol. Soc. Am. Spec. Papers 383.

Schellart, W.P., Freeman, J., Stegman, D., Moresi, L. & May, D., 2007. Evolution and diversity of subduction zones controlled by slab width, *Nature,* **446,** 308–311.

Scholz, C. & Campos, J., 1995. On the mechanism of seismic decoupling and back arc spreading at subduction zones, *J. geophys. Res.,* **100**(B11), 22 103–22 115.

Sdrolias, M. & Muller, R., 2006. Control on back-arc basin formation, *Geochem. Geophys. Geosyst.,* **7**(4), doi:10.1029/2005GC001090.

Shemenda, A.I., 1993. Subduction of the lithosphere and back-arc dynamics: insights from physical modeling, *J. geophys. Res.,* **98,** 16 167–16 185.

Shemenda, A.I., 1994. *Subduction: Insights from Physical Modeling*, Masson edn, Kluwer Academic Publishers, Dordrecht.

Sobolev, S. & Babeyko, A., 2005. What drives the Andes orogeny?, *Geology,* **33,** doi:10.1130/G21557.1.

Stegman, D., Freeman, J., Schellart, W., Moresi, L. & May, D., 2006. Influence of trench width on subduction hinge retreat rates in 3-d models of slab rollback, *Geochem. Geophys. Geosyst.,* **7**(3), doi:10.1029/2005GC001056.

Stern, J.R. & Smoot, N.C., 1998. A bathymetric overview of the Mariana forearc, *The Island Arc,* **7,** 525–540.

Tovish, A. & Schubert, G., 1978. Island arc curvature, velocity of convergence and angle of subduction, *Geophys. Res. Lett,* **5,** 329–332.

Turcotte, D. & Schubert, G., 1982. *Geodynamics: Application of Continuum Physics to Geological Problems*, John Wiley and Sons, New York.

Underwood, P., 1983. Dynamic relaxation, in *Computational Methods for Transient Analysis*, pp. 245–265, eds Belytschko, T. & Hughes, T., Elsevier Sci., New York.

Uyeda, S. & Kanamori, H., 1979. Back-arc opening and the mode of subduction, *J. geophys. Res.,* **84,** 1049–1061.

Van Hunen, J., Van Den Berg, A.P. & Vlaar, N.J., 2000. A thermo-mechanical model of horizontal subduction below an overriding plate, *Earth. planet. Sci. Lett.,* **182,** 157–169.

Vogt, P.R., 1973. Subduction and aseismic ridges, *Nature,* **241,** 189–191.

Vogt, P.R., Lowrie, A., Bracey, D.R. & Hey, R.N., 1976. Subduction of aseismic ridges: effects on shape, seismicity and other characteristics of consuming plate boundaries, *Geol. Soc. Am. Spec. Paper,* **172**.

Yamaoka, K., Fukao, Y. & Kumazawa, M., 1986. Spherical shell tectonics: effects of sphericity and inextensibility on the geometry of the descending lithosphere, *Rev. Gephys.,* **24,** 27–55.